Astronomy & Astrophysics manuscript no. m101.paper.v210116
January 26, 2016
©ESO 2016

Radio polarization and magnetic field structure in M 101 ⋆

E.M. Berkhuijsen[1], M. Urbanik[2], R. Beck[1], and J.L. Han[3]

[1] Max-Planck-Institut für Radioastronomie, Auf dem Hügel 69, 53121 Bonn, Germany
e-mail: eberkhuijsen@mpifr-bonn.mpg.de
[2] Astronomical Observatory, Jagiellonian University, ul. Orla 171, 30-244 Kraków, Poland
[3] National Astronomical Observatories, Chinese Academy of Sciences, A20 Datun Road, Beijing 100012, China

Received 7 September 2015 / Accepted 4 January 2016

arXiv:1601.06171v1 [astro-ph.GA] 22 Jan 2016

ABSTRACT

We observed total and polarized radio continuum emission from the spiral galaxy M 101 at $\lambda\lambda$ 6.2 cm and 11.1 cm with the Effelsberg telescope. The angular resolutions are 2.′5 (=5.4 kpc) and 4.′4 (=9.5 kpc), respectively. We use these data to study various emission components in M 101 and properties of the magnetic field. Separation of thermal and non-thermal emission shows that the thermal emission is closely correlated with the spiral arms, while the non-thermal emission is more smoothly distributed indicating diffusion of cosmic ray electrons away from their places of origin. The radial distribution of both emissions has a break near R = 16 kpc (=7.′4), where it steepens to an exponential scale length of $L \simeq 5$ kpc, which is about 2.5 times smaller than at $R < 16$ kpc. The distribution of the polarized emission has a broad maximum near R = 12 kpc and beyond R = 16 kpc also decreases with $L \simeq 5$ kpc. It seems that near R = 16 kpc a major change in the structure of M 101 takes place, which also affects the distributions of the strength of the random and ordered magnetic field. Beyond R=16 kpc the radial scale length of both fields is about 20 kpc, which implies that they decrease to about 0.3 μG at R = 70 kpc, which is the largest optical extent. The equipartition strength of the total field ranges from nearly 10 μG at $R < 2$ kpc to 4 μG at R = 22 − 24 kpc. As the random field dominates in M 101 ($B_{\rm ran}/B_{\rm ord} \simeq 2.4$), wavelength-independent polarization is the main polarization mechanism. We show that energetic events causing H I shells of mean diameter < 625 pc could partly be responsible for this. At radii < 24 kpc, the random magnetic field depends on the star formation rate/area, $\Sigma_{\rm SFR}$, with a power-law exponent of $b = 0.28 \pm 0.02$. The ordered magnetic field is generally aligned with the spiral arms with pitch angles that are about 8° larger than those of H I filaments.

Key words. Galaxies: individual: M 101 – galaxies: magnetic fields – galaxies: star formation – polarization - radio continuum: galaxies – radiation mechanisms: non-thermal

1. Introduction

The Pinwheel galaxy, M 101 (NGC 5457) is a nearby spiral galaxy seen nearly face-on (see Table 1). It is an SAB(rs)cd galaxy (de Vaucouleurs et al. 1976) containing many H II regions and several large H II complexes. Sensitive optical imaging of Mihos et al. (2013) showed that in blue light the bright parts of M 101 have a radius of about 8′on the sky (R_{25} = 8′), but that a weak optical disk can be traced about three times further out ($R_{29.5}$ = 25′). However, the galaxy is strongly lopsided, which may be due to past encounters with one or more of the six companions forming the M 101 group (e.g. Karachentsev & Kudrya 2014; Mihos et al. 2013; Jog & Combes 2009; Waller et al. 1997). The distance to M 101 has been the subject of many optical studies. We have adopted the Cepheid distance of $D = 7.4 \pm 0.6$ Mpc derived by Kelson et al. (1996), which is in good agreement with the compilation and new measurements of Lee & Jang (2012). Some basic parameters of M 101 relevant to our work are listed in Table 1.

M 101 has been observed at many wavelengths. High-resolution maps have been presented in the emission lines of atomic hydrogen (H I) (Kamphuis 1993; Braun 1995; Walter et al. 2008), CO(1-0) (Kenney et al. 1991; Helfer et al. 2003) , and ionized hydrogen (Hα) (Scowen et al. 1992; Hoopes et al. 2001), as well as of the emission in far-ultraviolet (FUV) (Waller et al. 1997), X-rays (Kuntz et al. 2003), and mid-infrared (mid-IR) (Jarrett et al. 2013). These maps show a complicated structure of many narrow, patchy spiral arms with large variations in pitch angle. The many linear arm segments and the asymmetry of the large-scale structure are attributed to a collision with the satellite galaxy NGC 5474 (Waller et al. 1997; Kamphuis 1993; Mihos et al. 2012). Kenney et al. (1991) detected a bar in the centre in CO, which is also seen in Hα and near-infrared (NIR), but density waves are weak in M 101 (Kamphuis 1993).

Little is known about the magnetic field in M 101. The first radio contiunum maps were presented by Israel et al. (1975) who used aperture synthesis at wavelengths $\lambda\lambda$ 49.2, 21.2, and 6 cm showing enhanced emission from spiral arms and H II-region complexes. Gräve et al. (1990) carried out a multi-wavelength study of M 101 at $\lambda\lambda$ 11.1, 6.3, 2.8, and 1.2 cm with the 100 m telescope at Effelsberg, leading to the first spectral index map of the galaxy. At λ 6.3 cm they also obtained the first map of polarized emission from M 101, indicating the existence of an ordered, large-scale magnetic field generally oriented along spiral arms. However, the sensitivity of these data were insufficient for further analysis of the field properties.

We observed M 101 with the Effelsberg telescope at $\lambda\lambda$ 6.2 and 11.1 cm with improved sensitivity in total power and polarization. Our data allow a detailed study of the properties of the magnetic field in M 101 after separation of the thermal (free-free) and non-thermal (synchrotron) components of the radio

⋆ Based on observations with the 100 m telescope of the MPIfR at Effelsberg

Table 1. Adopted parameters on M 101

Variable	Value	Reference
Distance D (Mpc)	7.4 ($1' = 2.15$ kpc)	Kelson et al. (1996)
Centre position		
$(RA,Dec)_{2000}$	$14^h\,03^m\,12\overset{s}{.}77, 54^\circ\,20'\,54\overset{''}{.}4$	Israel et al. (1975)
Position angle PA	38°	Kamphuis (1993)
Inclination i^a	30° (face-on $i = 0^\circ$)	Kamphuis (1993)
Radius in colour B: R_{25}	$8'$	Mihos et al. (2013)
Radius in colour B: $R_{29.5}$	$25'$	Mihos et al. (2013)
Radius in H I	$27'$	Kamphuis (1993)
Hubble type	SAB(rs)cd	de Vaucouleurs et al. (1976)

Notes. [(a)] Kamphuis derived different inclination angles for radii $R < 7'$ (27°) and $R > 7'$ (25° in SW and 40° in NE). As our data extend to $R \sim 15'$, we adopted a mean value of $i = 30^\circ$.

continuum emission. In this paper, we study the strength and regularity of the magnetic field, depolarization effects and their origin, the influence of star formation on the strength of the random field, and the relationship between the orientation of the ordered field and spiral arms.

The observations and reduction procedures are described in Sect. 2. In Sect. 3.1 we present the resulting maps and in Sect. 3.2 we separate thermal/non-thermal emission and derive radial scale lengths of the various emission components. The discussion in Sect. 4 consists of several parts. Sect. 4.1 shows the radial distribution of the magnetic field strengths and the dependence of the random field on the star formation rate (SFR); Sect. 4.2 discusses Faraday rotation measures and depolarization effects in M 101; Sect. 4.3 describes the large-scale structure of the ordered magnetic field, the alignment with H I arms, and a model to explain the alignment. Finally, we summarize our conclusions in Sect. 5.

2. Observations and data reduction

M 101 was observed at the frequencies 2.7 GHz (λ 11.1 cm) and 4.85 GHz (λ 6.2 cm) with receiver systems in the 100 m Effelsberg telescope between July and December 1997. At these frequencies the half-power beamwidths are $4\overset{'}{.}4$ and $2\overset{'}{.}5$, respectively. The system parameters are listed in Table 2. The point sources 3C 286 and 3C 138 were observed for calibrations of flux density and polarization angle. We adopted $S_{11} = 5.8$ Jy and $S_6 = 3.8$ Jy for 3C 138, and $S_{11} = 10.4$ Jy and $S_6 = 7.5$ Jy for 3C 286, respectively (Ott et al. 1994; Fernini et al. 1997).

We observed a large field of $51' \times 51'$ at λ 11.1 cm to enable proper base level determination. The field was centred on the galaxy (see Table 1) and alternately scanned in RA and DEC. We used a single horn, a scan speed of $60'$ per minute, and a scan separation of $1.5'$ in DEC (or RA) between scans, which is about one-third of the beamwidth, as needed for complete sampling of the emission. We obtained 14 coverages, half of which were scanned in RA and the other half in DEC. Each coverage took about 40 minutes.

We carried out the data processing with the NOD2 package (Haslam 1974). After removal of strong interference and adjustment of base levels of individual scans, final maps in Stokes I, Q, and U were made with the baseline optimizing procedure described by Emerson & Gräve (1988). After combining all coverages, we reached noise levels of $\sigma_{\rm I} = 1.20$ mJy/beam area and $\sigma_{\rm PI} = 0.54$ mJy/beam area for the maps of total intensity (I) and polarized intensity ($PI = \sqrt{Q^2 + U^2}$), respectively. Finally, the PI map was corrected for positive noise bias (Wardle & Kronberg 1974).

Table 2. System parameters

	λ 11.1 cm	λ 6.2 cm
Feed	Single horn	Dual horn
System Temperature (K)	45	30
Centre Frequency (GHz)	2.7	4.85
Bandwidth (MHz)	40	300
Half-power beamwidth	$4\overset{'}{.}4$	$2\overset{'}{.}5$
$\sigma_{\rm I}$ (mJy/beam area)	1.20	0.50
$\sigma_{\rm PI}$ (mJy/beam area)	0.54	0.07

We observed the same field at λ 6.2 cm as at λ 11.1 cm, using the dual-horn system. Because the beams of the two horns are separated by $8\overset{'}{.}12$ in azimuth, the galaxy can only be scanned in azimuth. With a scan speed of $60'$ per minute and a scan separation in elevation of $1'$, one coverage took about 51 minutes. In all, we obtained 20 coverages.

The dual-horn system is less sensitive to interference and weather changes than the single-horn system because disturbances are largely removed in the difference (i.e. time aligned and then subtracted) maps of the two horns. During data processing with NOD2, we removed residual interference from the difference I, Q, and U maps, adjusted the base level of each scan, restored the sky map from the difference maps using the method by Emerson et al. (1979), and transformed the maps to equatorial coordinates. Maps from all coverages were then combined to the final I, Q, and U maps using the NOD2 routine TURBOPLAIT. We reached a noise level of $\sigma_{\rm I} = 0.50$ mJy/beam area for the I map and of $\sigma_{\rm PI} = 0.07$ mJy/beam area for the PI map, which is nearly three times better in I and more than ten times better in PI than was obtained by Gräve et al. (1990). Again, the PI map was corrected for positive noise bias (Wardle & Kronberg 1974). The estimated error in the absolute flux-density scale is 5 percent and instrumental polarization in the extended emission is negligible.

3. Results

3.1. Total emission and polarized emission

The distribution of the total radio emission from M 101 at λ 6.2 cm (Fig. 1) is asymmetric. The eastern half has a steep brightness gradient towards the outside, while in the western half the emission falls off more gradually beyond the western spiral arms. This reflects the optical asymmetry in M 101 with the western arms extending to a considerably larger radius

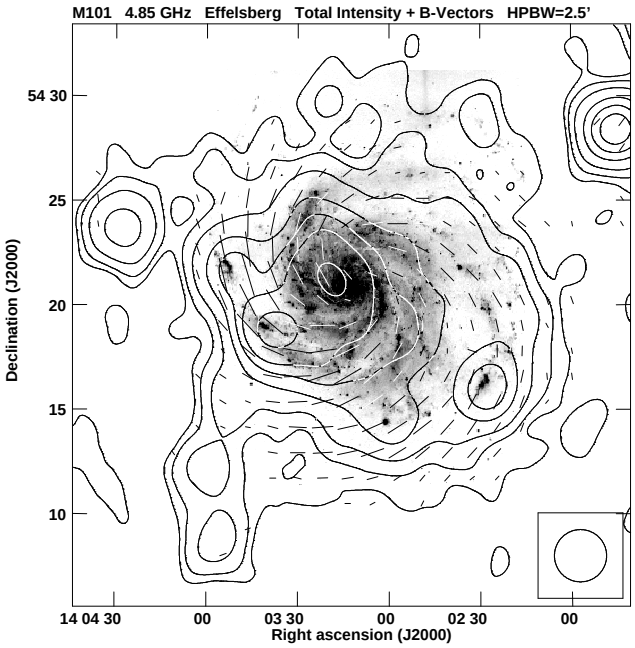

Fig. 1. Total emission and apparent B-vectors of the polarized emission (defined as E-vectors rotated by 90°) from M 101 observed at λ 6.2 cm overlaid on the optical image of Sandage (1961). The contour levels are 1, 2, 4, 8, 12, 16, and 24 mJy/beam area . A vector of 1′ length corresponds to a polarized intensity of 1 mJy/beam area . The noise levels are 0.5 mJy/beam area in *I* and 0.07 mJy/beam area in *PI*. The beamwidth of 2.′5 is shown in the lower right corner. A square-root scale has been applied to the optical image to show low surface brightness structures more clearly.

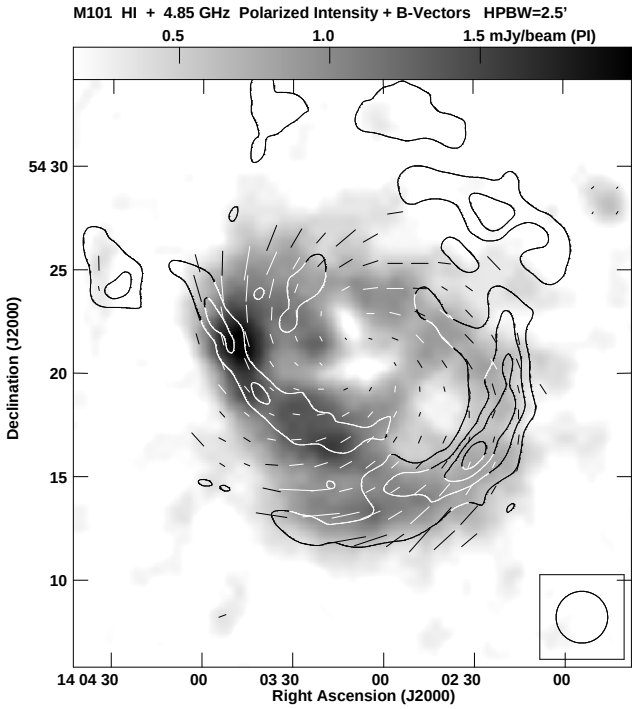

Fig. 2. Greyscale plot of the observed intensity of polarized emission from M 101 at λ 6.2 cm and apparent B-vectors (E+90° , not corrected for Faraday rotation) with length proportional to the degree of polarization. A vector of 1′ length corresponds to 20%. The noise level in PI is 0.07 mJy/beam area . Contours show the brightness distribution of H I of Braun (1995). The contour levels of column density are (10, 15, 20, and 25) 10^{20} cm $^{-2}$. The beamwidth of 2.′5 is shown in the lower right corner.

than the eastern arms. The maximum located 1.′5 NE of the centre coincides with background source number 20 in the list of Israel et al. (1975); the emission from the nucleus is much weaker. Other brightness peaks coincide with large star-forming complexes in the western arms as well as with two large complexes in the eastern arms and the giant H II region NGC 5471 at RA=$14^h\,04^m\,28\overset{s}{.}6$, Dec=54° 23′ 40.″3. The south-eastern extension has no optical counterpart; inspection of a larger field in the digitized sky survey (DSS) and of the deep survey of Mihos et al. (2013) did not show any optical emission along this feature. It consists of several background sources unrelated to M 101. Checking the catalogue of faint images of the radio sky at twenty cm (FIRST), we found two compact sources coinciding with the upper maximum in the extension and three sources with the lower maximum. The strong source in the north-west on the edge of the field also is a background source.

The asymmetry in total emission and the extension towards the south are also visible in the map at λ 11.1 cm (Fig. 3). The extended maximum near the centre is clearly displaced from the nucleus because of the background source mentioned before. In the western disk, the radio contours show some emission enhancement at the position of a large star-forming complex in the spiral arm; the emission is also enhanced on NGC 5471.

The distribution of polarized emission from M 101 at λ 6.2 cm shows the same east-west asymmetry as the total emission (Fig. 2). The brightest peak is located at 5′ east of the optical centre on the inside of the outer eastern arm. The innermost disk is depolarized by various effects (see Sect. 4.2.1). The size of the southern part of this minimum corresponds to the area below the central bar and innermost spiral arms seen in Hα (Scowen et al. 1992) and CO (Kenney et al. 1991), while the upper part of the minimum is on a crossing of several thin arms just north of the innermost arm Another depression in the polarized intensity occurs about 5′ south-west of the centre. It does not correspond to any particular optical or Hα feature, but coincides with an extended minimum in the H I map of Braun (1995) between two major spiral arms.

The apparent polarization B-vectors (defined as observed E-vectors rotated by 90°) at λ 6.2 cm form a very regular spiral pattern (Figs. 1 and 2). Despite the moderate resolution, the apparent magnetic field orientations follow the optical spiral arms. The same magnetic pattern is observed at λ 11.1 cm (Fig. 3). The similar orientations of the vectors suggest that Faraday rotation between these frequencies is small (see Sect. 4.2.1).

3.2. Thermal and non-thermal emission

Before further analysing our data, we subtracted four unrelated point sources from the total power maps at $\lambda\lambda$ 6.2 and 11.1 cm. We then smoothed the λ 6.2 cm maps in *I* and *PI* to a beamwidth of 2.′7 and those at 11.1 cm to 5.′0, which improved the sensitivities at λ 6.2 cm to $\sigma_{\rm I}(\sigma_{\rm PI})$ = 0.460 (0.065) mJy/beam area and at λ 11.1 cm to $\sigma_{\rm I}$ ($\sigma_{\rm PI}$) = 1.05 (0.47) mJy/beam area .

For the separation of thermal and non-thermal components of the total emission we need a map of the total spectral index α and the non-thermal spectral index $\alpha_{\rm n}$ [1]. Gräve et al. (1990) derived a spectral index map between $\lambda\lambda$ 49.2 cm and 2.8 cm at 1.′5 resolution (see their figure 5a). After smoothing the $\lambda\lambda$ 49.2 cm and 2.8 cm maps to the resolutions of 2.′7 and 5.′0, which considerably reduced the noise, we calculated maps of total spectral

[1] We use the convention $S \propto \nu^{-\alpha}$

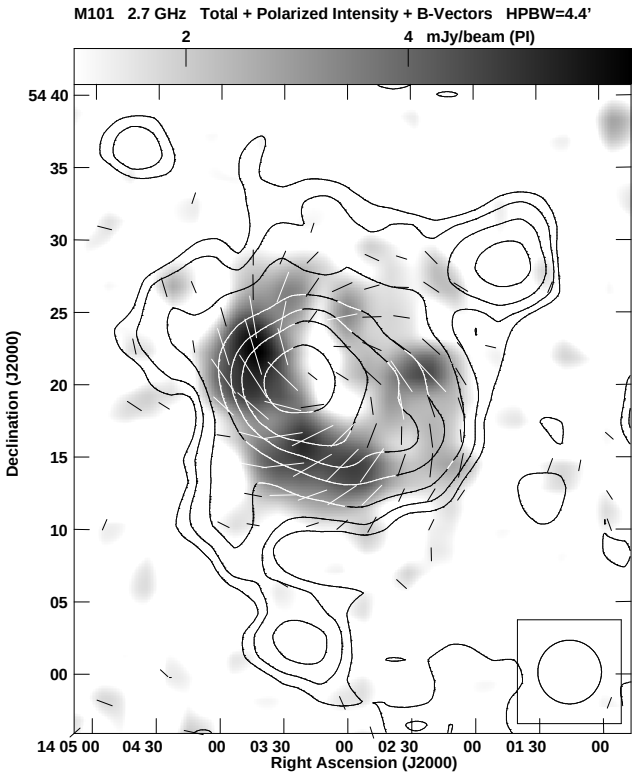

Fig. 3. Distribution of the total emission and apparent B-vectors (E+90°, not corrected for Faraday rotation) of polarized emission from M 101 observed at λ 11.1 cm, overlaid on a greyscale image of the polarized intensity. Contour levels are 3, 6, 12, 24, 36, 48, and 72 mJy/beam area, a vector of 1′ length corresponds to a polarized intensity of 1.5 mJy/beam area. The noise levels are 1.2 mJy/beam area in I and 0.54 mJy/beam area in PI. The beamwidth of 4.′4 is shown in the lower right corner.

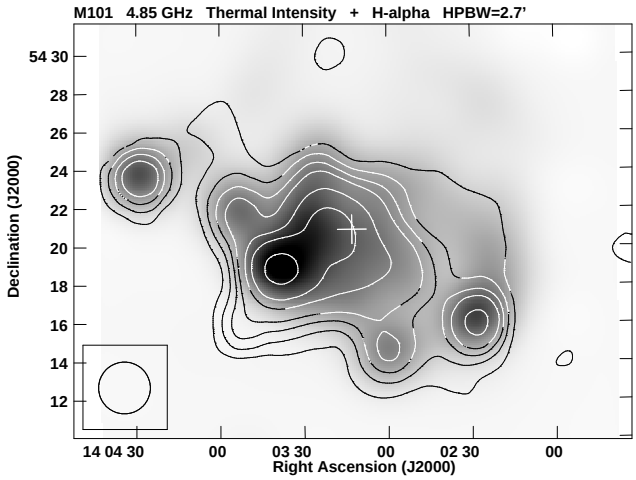

Fig. 4. Distribution of the thermal radio emission from M 101 at λ 6.2 cm overlaid on a greyscale plot of the Hα emission of Hoopes et al. (2001) smoothed to the same beamwidth of 2.′7 (shown in the lower left corner). Contour levels are (1, 2, 3, 4, 6, 8, and 12) × 1.5 mJy/beam area. The noise level is about 0.5 mJy/beam area. The white plus shows the position of the optical centre. The strong source near the eastern border of the map is the H II-region complex NGC 5471.

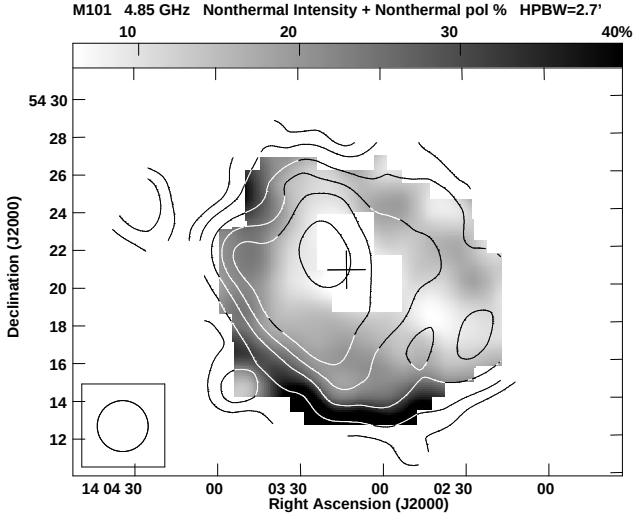

Fig. 5. Distribution of the non-thermal emission from M 101 at λ 6.2 cm (contours) superimposed onto the non-thermal degree of polarization (greyscale). Contour levels are 1, 2, 4, 6, 8, and 12 mJy/beam area. The centre position is indicated with a plus. The maximum in the emission NE of the centre is due to the background source number 20 in the list of Israel et al. (1975). The noise level in the non-thermal intensity is about 0.5 mJy/beam area. In the centre region, strong depolarization causes very low non-thermal polarization degrees. The beamwidth is 2.′7.

index at our resolutions for all points above the noise level in both maps. The spectral index varies from about 0.6 in the inner part to 0.9 or 1.0 at large radii. The large difference in λ between the maps and the low noise yield errors in the α map of < 0.02 within 7 arcmin from the centre, which slowly increase to < 0.1 further out.

Gräve et al. (1990) determined α and $\alpha_{\rm n}$ with the method described by Klein et al. (1984), using the integrated flux densities for $R < 14'$ at ten frequencies. They found $\alpha = 0.72 \pm 0.04$ and $\alpha_{\rm n} = 0.92 \pm 0.18$. Furthermore, Gräve et al. (1990) observed that α becomes about 0.9 in the outer parts of M 101 where all the emission is non-thermal, and they found that after subtraction of the bright H II regions α also becomes about 0.9 in the inner parts. So $\alpha_{\rm n}$ must be close to 0.9. Following Gräve et al. (1990), we integrated our $\lambda\lambda$ 6.2 and 11.1 cm maps over the area $R < 14'$, yielding $S_6 = 310 \pm 20$ mJy and $S_{11} = 480 \pm 30$ mJy. These values are less than 8% lower than those listed by Gräve et al. (1990) but agree within errors. Therefore we adopted the value of $\alpha_{\rm n} = 0.92 \pm 0.10$ for our study.

For the separation of thermal/non-thermal emission only pixels in the spectral index map with realistic values of α were used. If $\alpha \leq 0.1$ the emission is fully thermal and fully non-thermal if $\alpha \geq \alpha_{\rm n}$; elsewhere the thermal fraction is calculated. The resulting thermal emission is then subtracted from the total emission to obtain the non-thermal emission. In Sect. 3.2.1 we discuss how thermal and non-thermal emission depend on the uncertainty of 0.1 in $\alpha_{\rm n}$.

In Fig. 4 we compare the distribution of thermal emission at λ 6.2 cm with that of the Hα emission (Hoopes et al. 2001) smoothed to the same beam size. Maxima in the radio thermal emission from M 101 agree well with those in the Hα emission.

In Fig. 5 we show the distribution of the non-thermal emission from M 101, NTH, at λ 6.2 cm (contours) superimposed onto the degree of non-thermal polarization $p_{\rm n} = PI/NTH$ (greyscale). The NTH has a larger extent than the thermal emission, especially to the north. The strong emission 1.′5 NE of the centre is from the background source number 20 listed by Israel et al. (1975); the emission from the nucleus itself is very weak. The NTH is slightly enhanced on the brightest spiral arms

Table 3. Integrated flux densities of M 101 for $R < 14'$ (=30 kpc)

Component	λ 6.2 cm	Systematic error
I (mJy)	310 ± 20	—
TH (mJy)	140 ± 15	±30
$f_{\rm th}$	0.45 ± 0.06	±0.1
NTH (mJy)	170 ± 15	±30
PI (mJy)	28 ± 3	—
$p_{\rm n}$	0.16 ± 0.02	±0.03

Notes. Errors in column 2 are statistical errors; those in column 3 arise from an uncertainty of 0.10 in $\alpha_{\rm n}$ (see Sect. 3.2.1).

and on the star formation complex in the south-west, which is visible in Fig. 4. The values of $p_{\rm n}$ gradually increase from the centre outwards and degrees of more than 40% are reached in the south. On the star formation complex in the south-west, $p_{\rm n}$ has a minimum of < 10%.

The integrated flux densities of the thermal (TH), NTH, and polarized (PI) emission at λ 6.2 cm are listed in Table 3, together with the average thermal fraction $f_{\rm th} = TH/I$ and the mean value of $p_{\rm n} = PI/NTH$. About 50% of the TH comes from the five giant H II region complexes observed by Israel et al. (1975). The flux density of TH and $f_{\rm th}$ may be overestimated by 20–25% because we used a constant value of $\alpha_{\rm n}$, which is too large for star-forming regions (Tabatabaei et al. 2007a, 2013a). In this case, NTH ($p_{\rm n}$) is underestimated (overestimated) by nearly 20%. For further interpretation, a more realistic separation of thermal/non-thermal emission is required, i.e. by determining the thermal emission from extinction-corrected Hα data, which does not need the assumption of a constant value of $\alpha_{\rm n}$ throughout the galaxy (Tabatabaei et al. 2007a).

The radial distributions of I and the emission components in M 101 at λ 6.2 cm are shown in Fig. 6. The deep central minimum in PI is clearly visible, but NTH and TH similarly decrease with increasing radius. We do not show TH and NTH points for $R > 24$ kpc because at these large radii the TH and NTH maps are no longer complete, which make the radial averages unreliable. In each of the curves a break is visible near $R = 16$ kpc. Therefore, we separately determined exponential radial scale lengths L for the intervals $R = 0 - 16$ kpc, $R = 16 - 24$ kpc and $R = 16 - 30$ kpc (for I and PI) by fitting the intensities, weighted by their errors, to $I(R) = a \cdot \exp(-R/L)$. For PI only L at large R could be determined. The resulting scale lengths are given in Table 4. At $R = 0 - 16$ kpc, NTH decreases more slowly ($L = 13.0 \pm 1.4$ kpc) than TH ($L = 10.2 \pm 1.0$ kpc), as is expected if cosmic ray electrons diffuse away from their birth places in star-forming regions. However, beyond $R = 16$ kpc all three components have the same radial scale length of $L \simeq 5$ kpc, suggesting that in the outer disk the cosmic ray electrons escape into the halo of M 101.

Mihos et al. (2013) found a change in the radial scale length of the optical surface brightness at $R = 7' - 9'$, which is the same radius as the break in the radio profiles. This position near $R = 16$ kpc (=7.′4) corresponds to the radius where the inclination angle changes and the H I gas starts deviating from differential rotation (Kamphuis 1993). Beyond $R = 7'$ the gas starts flaring with velocity components perpendicular to the midplane of M 101.

The change in scale length near $R = 16$ kpc, which is seen in the distributions of thermal and non-thermal radio emission and optical surface brightness, is accompanied by a change in the velocity structure near the same radius. Taken together, these

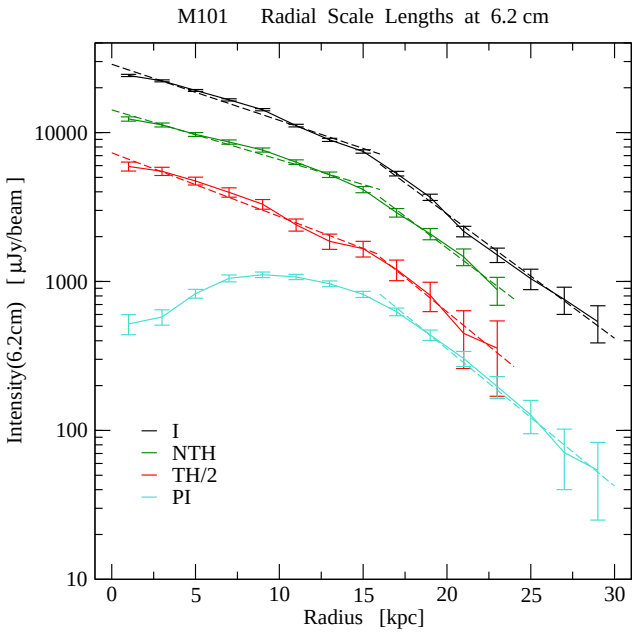

Fig. 6. Average intensity in 2 kpc-wide rings in the plane of M 101 of I and the emission components NTH, TH and PI plotted against galactocentric radius. For clarity, intensities of TH are halved. Errors are standard deviations. Note the change in the slopes near R=16 kpc. Dashed lines show the fits giving the exponential radial scale lengths listed in Table 4.

phenomena indicate a major change in the structure of M 101 near R=16 kpc.

A break in the scale length of the radio continuum emission near the radius where the star formation vanishes has also been found in M 33 (Tabatabaei et al. 2007b), M 51 (Mulcahy et al. 2014) and IC 342 (Beck 2015). The IR emission from M 33 also shows a break at this radius. Hence, a break in the radial scale length of emission components near the radius where the star formation comes to an end may be a general phenomenon in galaxies.

3.2.1. The effect of an error in $\alpha_{\rm n}$ on TH and NTH

We repeated the thermal/non-thermal separation for $\alpha_{\rm n} = 0.82$ and $\alpha_{\rm n} = 1.02$ to investigate how sensitive TH and NTH are to the error in $\alpha_{\rm n}$. Figure 7 shows the radial variation of the thermal emission for these cases and for $\alpha_{\rm n} = 0.92$. The difference from our standard case is typically 20%, hence, the error in $\alpha_{\rm n}$ causes a systematic error of 20% in TH and a similar error in NTH. As the non-thermal degree of polarization is $p_{\rm n} = PI/NTH$, $p_{\rm n}$ also has a 20% systematic error (see Table 3). The resulting systematic errors in the scale lengths are given in Table 4.

In Fig. 7 we also show the radial profile of the Hα emission observed by Hoopes et al. (2001), scaled to TH for $\alpha_{\rm n} = 0.92$ at $R = 16 - 18$ kpc. Apart from the inner 6 kpc the profiles are almost identical. The discrepancy near the centre is due to the combination of extinction in Hα and a possible overestimate of TH on the many H II regions in this area in M 101. This comparison, and the overlay in Fig. 4, show that our thermal/non-thermal separation yields a good estimate of the distribution of the thermal emission in the galaxy.

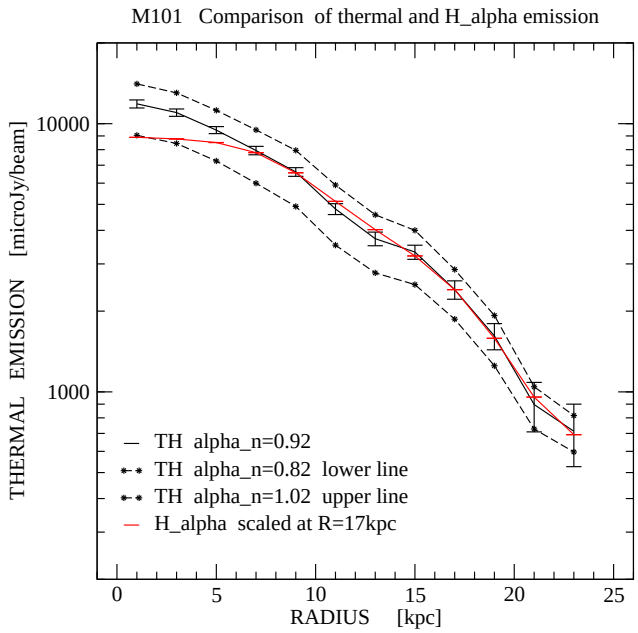

Fig. 7. Average intensity in 2 kpc-wide radial rings in the plane of M 101 of TH derived with $\alpha_n = 0.92$ (solid line) and with $\alpha_n = 0.82$ and 1.02 (dotted lines), plotted against galacto-centric radius. The errors on the dotted lines are the same as on the solid line, but are not shown for clarity. The red line shows the radial distribution of the Hα emission (Hoopes et al. 2001), scaled to TH derived with $\alpha_n = 0.92$ at the ring $R = 16 - 18$ kpc. Note the close corresponcence between the two distributions at $R > 6$ kpc. The discrepancy in the central part may be due to extinction in Hα and a possible overestimate of TH on H II regions.

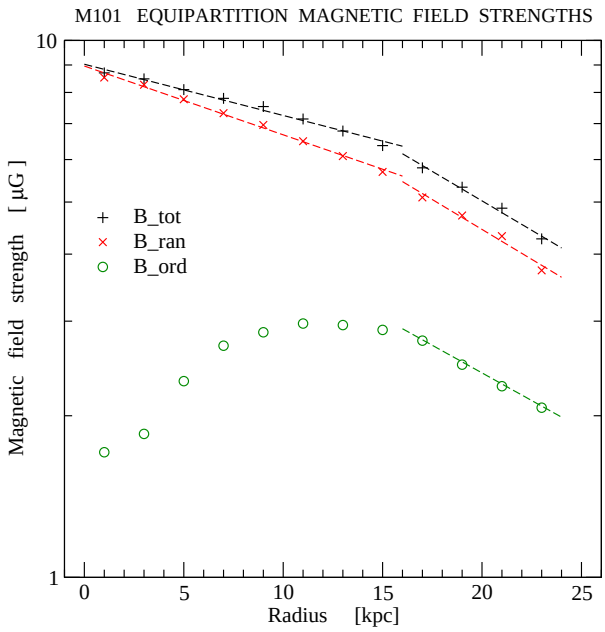

Fig. 8. Variation with galacto-centric radius of the equipartition magnetic field strengths B_{tot}, B_{ran}, and B_{ord} averaged in 2 kpc-wide rings in the plane of M 101. There is a change in slope near R=16 kpc. Dashed lines represent the exponential fits yielding the radial scale lengths given in Table 4

.

4. Discussion

We now employ the non-thermal and polarized emission components derived in the foregoing sections for an analysis of various properties of the magnetic field in M 101. We show how magnetic field strengths decrease with increasing distance to the centre and how the random magnetic field depends on the star formation rate per unit area, Σ_{SFR}. We discuss Faraday rotation measures and depolarization effects, and look at the large-scale structure of the ordered field.

4.1. Magnetic field strengths and star formation rate

4.1.1. Radial distribution of magnetic field strengths

From the radial variations of the surface brightnesses of NTH and PI at λ 6.2 cm presented in Fig. 6, we calculated the mean equipartition strengths of the total (B_{tot}), ordered (B_{ord}), [2] and random (B_{ran}) magnetic field using the code BFIELD of M. Krause based on equation (3) of Beck & Krause (2005). The code also requires the non-thermal spectral index α_n, the non-thermal degree of polarization p_n, the line of sight L_{nth} through the emitting medium, and the ratio of the energy densities of protons and electrons K, here taken as 100. We used $\alpha_n = 0.92$ (Sect. 3.2) and a scale height of the non-thermal emission of 1 kpc, leading to $L_{nth} = 2/cos(i) = 2.3$ kpc. Fig. 8 shows the radial distributions of B_{tot}, B_{ran}, and B_{ord} in 2 kpc-wide rings around the centre for $R < 24$ kpc. [3] The total field strength is nearly 10 μG near the centre and drops to about 4 μG in the ring $R = 22 - 24$ kpc. The mean field strengths in the area $R < 24$ kpc are $B_{tot} = 6.4\,\mu$G, $B_{ran} = 5.9\,\mu$G and $B_{ord} = 2.5\,\mu$G. With $B_{ran}/B_{ord} = 2.4$, the magnetic field in M 101 is highly random like in, for example IC 342 (Beck 2015).

In Fig. 8 the break in the slope of the curves near $R = 16$ kpc is very clear. Like in Sect. 3.2, we calculated the exponential radial scale lengths for the two intervals $R < 16$ kpc and $R = 16 - 24$ kpc. Table 4 shows that the magnetic fields have very long scale lengths of 34 – 45 kpc at $R < 16$ kpc and about 20 kpc at larger radii. In the inner region, B_{ord} is low due to the depolarization; therefore, the scale length of B_{tot} is significantly larger than that of B_{ran} ($(B_{tot})^2 = (B_{ran})^2 + (B_{ord})^2$). In the outer region, B_{ran} and B_{ord} have the same scale length. If this scale length remains the same out to the radius of the maximal observed optical extent of $R \simeq 70$ kpc (van Dokkum et al. 2014) and of the H I gas of the extension in the southwest of $R = 90$ pc (Mihos et al. 2012), the field strengths will have dropped to about 0.3 μG and 0.2 μG, respectively. Hence, the intragroup magnetic field strength is probably smaller than 0.3 μG, which is similar to the value estimated for a local group of irregular dwarf galaxies (Chyży et al. 2011).

[2] *Ordered* magnetic fields as traced by linearly polarized emission can be either *regular* fields, preserving their direction over large scales (leading to both polarized emission and rotation measure), or *anisotropic random* fields with multiple random field reversals within the telescope beam, caused by shear and/or compression of isotropic random fields (leading to polarized emission but not to rotation measure). To observationally distinguish between these fundamentally different types of magnetic field, additional Faraday rotation data is needed.

[3] As field strength scales with the power $1/(3 + \alpha_n)$ of K, L_{nth}, and NTH, errors in these quantities and observational errors in NTH have little effect on the derived field strengths. The uncertainty of 0.1 in $\alpha_n = 0.92$ leads to less than 2% changes in B_{tot} and B_{ran} at $R < 16$ kpc and less than 5% errors at larger radii. Only the systematic error in B_{ord} is about 17% due to the systematic error in p_n (see Sect. 3.2.1).

Table 4. Exponential radial scale lengths L [kpc] of surface brightness at λ 6.2 cm and magnetic field strength. Errors are statistical errors. The numbers immediately below NTH, TH, and the field strengths are systematic errors in case $\alpha_n = 1.02$ (first one) or 0.82 (second one), respectively. The ratio between the scale lengths of B_{tot} and NTH at $R = 16 - 24$ kpc is $(3 + \alpha_n)$, which is expected if p_n is constant. Because p_n increases at $R = 0 - 16$ kpc, the ratio between the scale lengths of B_{tot} and NTH is less than $(3 + \alpha_n)$.

	$R = 0 - 16$ kpc	$R = 16 - 24$kpc	$R = 16 - 30$ kpc
I	11.5 ± 1.0	4.7 ± 0.5	5.2 ± 0.3
NTH	13.0 ± 1.4	5.1 ± 0.7	—
	$+0.2 - 0.5$	$+0.2 - 0.2$	—
PI	—	5.1 ± 0.2	4.7 ± 0.3
TH	10.2 ± 1.0	4.7 ± 0.8	—
	$+0.1 - 0.3$	$+0.4 - 0.1$	—
B_{tot}	45.5 ± 3.6	19.8 ± 2.9	—
	$+2.3 - 3.3$	$+2.0 - 1.5$	—
B_{ran}	33.9 ± 1.9	19.5 ± 3.6	—
	$-1.2 + 0.2$	$+2.8 - 1.8$	—
B_{ord}	—	21.1 ± 0.8	—
	—	$-1.7 + 0.6$	—

4.1.2. Dependence of magnetic field strength on star formation rate

Since supernova explosions, SNRs, and stellar winds are the principal actors stirring up the ISM, and hence producing random magnetic fields, a relationship between the random magnetic field B_{ran} and the mean star formation rate per unit area, Σ_{SFR}, is expected. This has indeed been found for the galaxies NGC 4254 (Chyzy 2008) and NGC 6946 (Tabatabaei et al. 2013b) as well as for the global values of a sample of nearby galaxies (e.g. Heesen et al. (2014)). Below we show that a relationship also exists in M 101.

As thermal radio emission is free-free emission from gas ionized by massive stars, the present-day Σ_{SFR} is proportional to the thermal surface brightness. Therefore, we evaluated the mean value of Σ_{SFR} in M 101 by comparing the thermal surface brightness at λ 21 cm, s_{21}, with that of M 33, for which Σ_{SFR} is known (see Berkhuijsen et al. 2013, table 6),

$$\Sigma_{SFR}(\mathrm{M\,101}) = \frac{s_{21}(\mathrm{M\,101})}{s_{21}\ (\mathrm{M\,33})}\,\Sigma_{SFR}(\mathrm{M\,33}). \quad (1)$$

At distance D we have $s_{21} = S_{21}\,4\,D^2\,/\,R^2$, where S_{21} is the thermal flux density of the area within radius R. With $D = 7.4$ Mpc, $S_{21} = TH_{21} = 160 \pm 13$ mJy within $R = 30$ kpc (calculated from TH_6 in Table 3) for M 101 and $D = 0.84$ Mpc, $S_{21} = 420$ mJy within $R = 5$ kpc and $\Sigma_{SFR} = 3.0 \pm 0.6\,M_\odot\,Gyr^{-1}\,pc^{-2}$ for M 33, we find $\Sigma_{SFR}(\mathrm{M\,101}) = 2.5 \pm 0.2\,M_\odot\,Gyr^{-1}\,pc^{-2}$ for the area $R < 30$ kpc ($R \lesssim 14'$). We then used the λ6 cm thermal map of M 101 to find the mean $\Sigma_{SFR,j}$ in the 2 kpc-wide rings used before

$$\Sigma_{SFR,j} = \frac{TH_{6,j}}{TH_6}\,\Sigma_{SFR}(\mathrm{M\,101}), \quad (2)$$

where $TH_{6,j}$ and TH_6 are the mean thermal intensity for ring j and $R < 30$ kpc, respectively. We present $\Sigma_{SFR,j}$ as a function of radius in Fig. 9. Since $\Sigma_{SFR} \propto TH$, the shape of the curve is the same as that of TH in Fig. 6. The thermal emission from M 101 has a systematic error of 20% because of the uncertainty in α_n (see Sect. 3.2.1); therefore, $\Sigma_{SFR}(\mathrm{M\,101})$ and $\Sigma_{SFR,j}$ also have a systematic error of 20%. The thermal emission and Σ_{SFR} of M 33, however, do not contain such a systematic error because they were both derived from extinction-corrected Hα data (Tabatabaei et al. 2007a; Berkhuijsen et al. 2013).

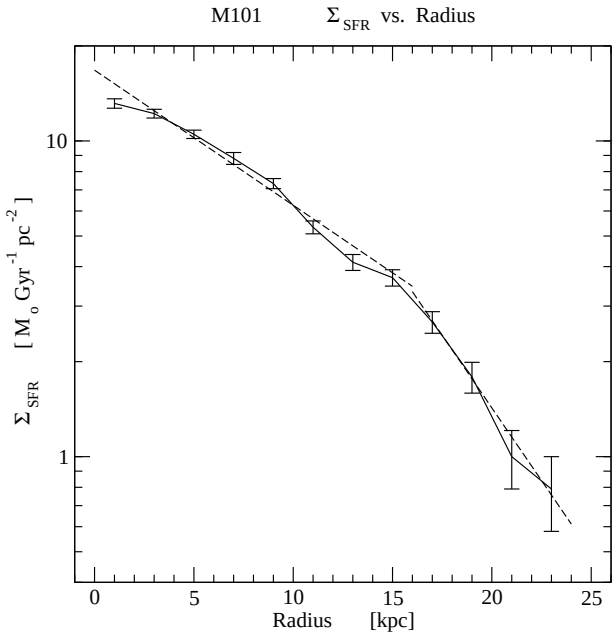

Fig. 9. Radial variation of the mean star formation rate per unit area, $\Sigma_{SFR,j}$, in 2 kpc-wide rings in the plane of M 101. The shape of the curve is the same as that of the thermal emission in Fig. 6. Errors are standard deviations. Dashed lines show the fits giving the scale lengths of TH in Table 4.

In M 101 the values of $\Sigma_{SFR,j}$ range from nearly $14\,M_\odot\,Gyr^{-1}\,pc^{-2}$ at $R < 2$ kpc to about $0.8\,M_\odot\,Gyr^{-1}\,pc^{-2}$ at $R = 22 - 24$ kpc, which is in good agreement with the range derived by Zasov & Abramova (2006, fig. 1) from UV and FIR data. Suzuki et al. (2010, fig. 8a) found values of $5 - 100\,M_\odot\,Gyr^{-1}\,pc^{-2}$ in spiral arms, and the map of Σ_{SFR} of Leroy et al. (2012, fig. 20) shows values of about $16\,M_\odot\,Gyr^{-1}\,pc^{-2}$ near the centre and of $0.6\,M_\odot\,Gyr^{-1}\,pc^{-2}$ in spiral arms. Hence, the radial distribution of $\Sigma_{SFR,j}$ in Fig. 9 is consistent with other estimates in the literature.

In Fig. 10 the mean values of B_{ran} in 2 kpc–wide rings are plotted against the corresponding mean values of Σ_{SFR} for $R = 0 - 24$ kpc. A power-law fit to the points yields

$$B_{ran} = (3.98 \pm 0.12)\,\Sigma_{SFR}^{0.28\pm0.02}. \quad (3)$$

The uncertainty in α_n causes a systematic error in the exponent of ≤ 0.02.

By using the values in 2 kpc-wide rings, our fit refers to a correlation on large scales. In spite of this, the exponent of 0.28 ± 0.02 is in good agreement with those found on small scales by Chyzy (2008) and Tabatabaei et al. (2013b), who derived exponents of 0.26 ± 0.01 for NGC 4254 and 0.16 ± 0.01 for NGC 6946, respectively, using pixel-to-pixel correlations. The small exponent found for NGC 6946 is attributed to the fast cosmic ray diffusion in this galaxy.

As discussed above, the radial distributions of magnetic field strength in Fig. 8 show a break near $R = 16$ kpc causing different scale lengths for $R < 16$ kpc and $R > 16$ kpc. We calculated the exponent b in $B \propto \Sigma_{SFR}^b$ from the scale lengths at $R < 16$ kpc and $R = 16 - 24$ kpc, given in Table 4, as $b = L_{SFR}/L_B$, where $L_{SFR} = L_{TH}$. As can be seen in Table 5, the values of b agree within errors. Although the power law between B_{ran} and Σ_{SFR} at $R <$

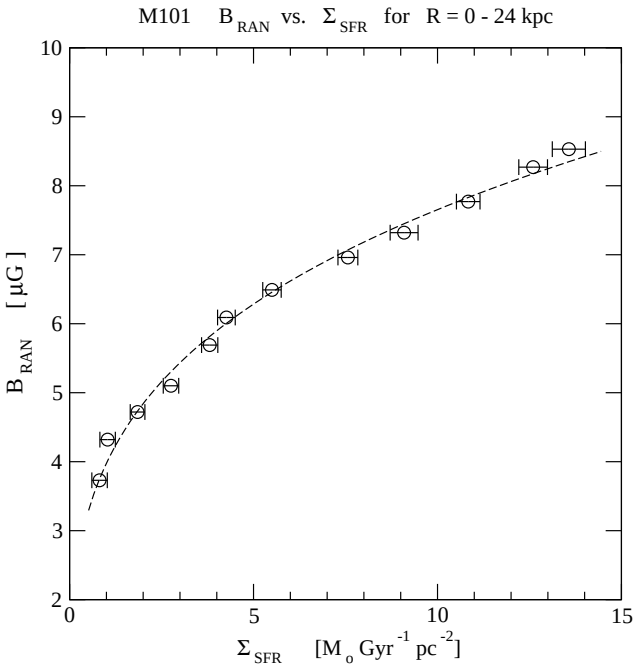

Fig. 10. Dependence of the turbulent magnetic field strength $B_{\rm ran}$ on the star formation rate per unit area, $\Sigma_{\rm SFR}$. The points represent average values in 2 -kpc wide rings in the plane of M 101. The dashed line shows the power-law fit for R <24 kpc given in the text. Statistical errors of 1 σ are shown for $\Sigma_{\rm SFR}$, but are negligble in $B_{\rm ran}$.

Table 5. Power-law exponents b in $B \propto \Sigma_{\rm SFR}^{b}$ from $b = L_{\rm SFR} / L_{\rm B}$. Systematic errors in b due to the uncertainty in $\alpha_{\rm n}$ are smaller than the statistical errors

Field type	$R = 0 - 16$ kpc	$R = 16 - 24$ kpc
$B_{\rm tot}$	0.22 ± 0.03	0.24 ± 0.05
$B_{\rm ran}$	0.30 ± 0.03	0.24 ± 0.07
$B_{\rm ord}$	——	0.22 ± 0.03

16 kpc may be somewhat steeper than that at $R = 16 - 24$ kpc, the fit for $R = 0 - 24$ kpc shown in Fig. 10 with $b = 0.28 \pm 0.02$ is within errors for both radial ranges. At $R > 16$ kpc, $B_{\rm ord}$ is also correlated with $\Sigma_{\rm SFR}$, which is not the case in NGC 4254 (Chyzy 2008) and NGC 6946 (Tabatabaei et al. 2013b). However, these authors used pixel-to pixel correlations for the whole galaxy, in which a possible weak dependence in the outer part may have been lost.

Since the total magnetic field contains a large random fraction, $B_{\rm tot}$ is correlated with $\Sigma_{\rm SFR}$ as well, but with a somewhat smaller exponent than $B_{\rm ran}$ (see Table 5). This is also the case in NGC 6946 (Tabatabaei et al. 2013b). Furthermore, significant correlations between the global values of $B_{\rm tot}$ and $\Sigma_{\rm SFR}$ have been found for a small sample of Local Group dwarfs with $b = 0.30 \pm 0.04$ (Chyży et al. 2011), for 17 low-mass, Magellanic-type and peculiar galaxies with $b = 0.25 \pm 0.02$ (Jurusik et al. 2014), for a sample of 17 galaxies with $b = 0.30 \pm 0.02$ (Heesen et al. 2014), and for a sample of 20 nearby spiral galaxies with $b = 0.19 \pm 0.03$ (Van Eck et al. 2015). It would be interesting to see if the observed variation in the exponent b could be related to the considerable variation in the dependence of the local star formation rate on the total gas surface density (Bigiel et al. 2008), on variations in the dependence of $B_{\rm tot}$ on the total gas volume density, and/or on variations in cosmic ray diffusion (fast diffusion causes a small exponent).

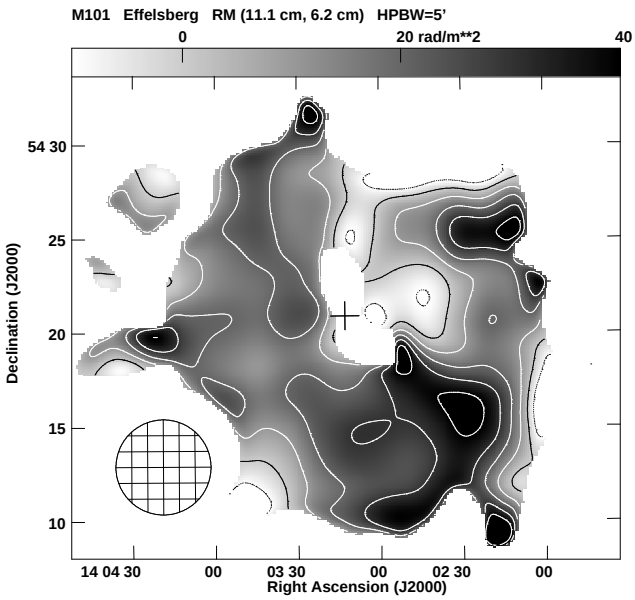

Fig. 11. Distribution of Faraday rotation measure $RM(11,6)$ (greyscale and contours) in M 101 between λ 11.1 cm and λ 6.2 cm. The data are convolved to a common beamwidth of 5′ shown in the lower left corner. Contour levels are -10, 0, 10, 20, 30, and 40 rad m^{-2} . The uncertainty in $RM(11,6)$ is about $10 - 15$ rad m^{-2} . The cross shows the centre of M 101.

4.2. Rotation measures and depolarization

In Fig. 11 we present the distribution of the Faraday rotation measures between λ 11.1 cm and λ 6.2 cm, $RM(11,6)$. After smoothing the PI(6 cm) map to the 5′ beamwidth of the PI map at 11 cm, $RM(11,6)$ was calculated for all data points above 2.3 times the noise in both maps. The ambiguity of 367 rad m^{-2} does not influence these results. East of the major axis $RM(11,6)$ varies smoothly around 20 rad m^{-2} , but in the western part strong gradients in $RM(11,6)$ occur. A comparison with Fig. 4 shows that $RM(11,6)$ is not correlated with the thermal emission from ionized gas that mainly originates from discrete H II regions with small volume filling factors. Only the maximum in $RM(11,6) > 40$ rad m^{-2} near the south-western major axis coincides with intense thermal emission. Hence, $RM(11,6)$ arises in the diffuse ionized gas in M 101. This is also the case in M 31 (Berkhuijsen et al. 2003) and M 51 (Fletcher et al. 2011).

The ratio of the non-thermal degree of polarization at λ 11.1 cm and λ 6.2 cm yields the Faraday depolarization between these wavelengths, $DP_{\rm n}(11,6) = p_{\rm n}(11) \,/\, p_{\rm n}(6)$, as the wavelength-independent polarization cancels. The uncertainty in $\alpha_{\rm n}$ causes a systematic error of 20% in $p_{\rm n}(6)$, 12% in $p_{\rm n}(11)$, and 10% in $DP_{\rm n}(11,6)$. The distribution of $DP_{\rm n}(11,6)$ across M 101 is shown in Fig. 12. $DP_{\rm n}(11,6)$ generally is close to unity, varying between about 0.7 and 1.3. This means that depolarization by Faraday effects is small. In Sect. 4.2.1 we estimate which depolarization mechanisms are important in M 101.

In comparing Fig. 11 and Fig. 12 one gets the impression that contour levels of RM are often perpendicular to contour levels of $DP_{\rm n}$. This is especially clear in Fig. 13 where both contour sets are shown. Contours of RM and $DP_{\rm n}$ tend to be perpendicular to each other at their crossing points. This suggests that gradients in RM are a significant cause of Faraday depolarization. This phenomenon was also observed in M 51 (Horellou et al. 1992) and M 31 (Berkhuijsen et al. 2003).

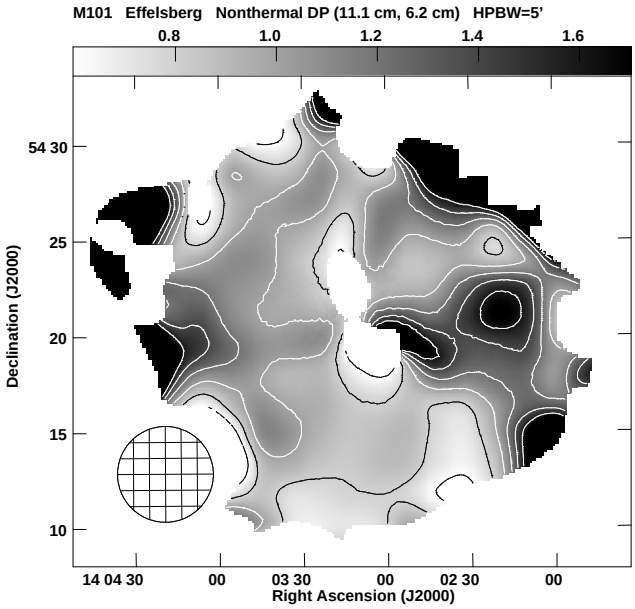

Fig. 12. Distribution of the non-thermal depolarization, $DP_{\rm n}(11,6)=p_{\rm n}(6)/p_{\rm n}(11)$, in M 101. Contour levels are 0.6, 0.8, 1.0, 1.2, 1.4, and 1.6. The uncertainty in $DP_{\rm n}(11,6)$ increases from 0.1 near the centre to 0.3 in the outer parts. The angular resolution is 5′.

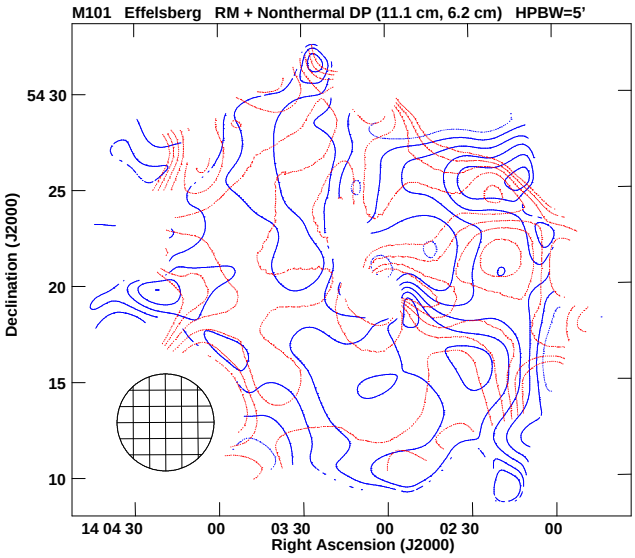

Fig. 13. Contours of $RM(11,6)$ (thick blue lines) and $DP_{\rm n}(11,6)$ (thin red lines) in M 101 superimposed. Thin and thick lines tend to be perpendicular to each other at their crossing points. The beamwidth is 5′.

4.2.1. Depolarization mechanisms in M 101

In order to understand which mechanisms are causing the depolarization in M 101, we calculated the mean values of $DP_{\rm n}(11,6)$ in 30° -wide sectors in two radial rings in the plane of the galaxy: an inner ring at $R = 2.'5 - 7.'5$ (= 5.4 – 16.1 kpc) and an outer ring at $R = 7.'5 - 12.'5$ (= 16.1 – 26.9 kpc). For the same sectors, we also calculated the mean values of $B_{\rm tot}$, $B_{\rm ran}$ and $B_{\rm ord}$, of $p_{\rm n}(6)$ and $p_{\rm n}(11)$, and of the intrinsic rotation measure, $RM_{\rm i}(11,6) = RM(11,6) - RM_{\rm f}$, where $RM_{\rm f}$ is the rotation measure of the Galactic foreground. We estimated $RM_{\rm f} = 15 \pm 5\,{\rm rad\,m^{-2}}$ from the mean $RM(11,6)$ in the two rings. The rotation measures of the three polarized point sources located within 30′ from the centre of M 101 vary between $2 \pm 10\,{\rm rad\,m^{-2}}$ and $9 \pm 6\,{\rm rad\,m^{-2}}$ (Oppermann et al. 2012), which is in fair agreement with our value of $RM_{\rm f}$. The azimuthal profiles for the two rings are shown in Fig. 14 and Fig. 15.

The profiles for the inner ring (Fig. 14) show little variation with azimuth. The non-thermal degrees of polarization $p_{\rm n}(6)$ and $p_{\rm n}(11)$ are nearly the same and $DP_{\rm n}(11,6)$ remains close to 1. Hence, Faraday depolarization is unimportant and the low values of $p_{\rm n} \simeq 0.1$ must be due to wavelength-independent polarization [4]. The top panel shows that in all sectors $B_{\rm ran}$ dominates as $B_{\rm ran}/B_{\rm ord} \simeq 2.5$ and $B_{\rm ran}/B_{\rm tot} \simeq 0.9$. $RM_{\rm i}(11,6)$ (bottom panel) is generally small, but changes from $\simeq 15\,{\rm rad\,m^{-2}}$ to $\simeq -15\,{\rm rad\,m^{-2}}$ between $Az = 210°$ and $Az = 240°$. Figure 11 shows a strong gradient in $RM(11,6)$ in these sectors, which causes the depression in PI south-west of the centre in Fig. 2. This area is coincident with an extended minimum in the H I map of Braun (1995).

In the outer ring (Fig. 15) the situation is more complex. From $Az = 90°$ to $Az = 180°$, the non-thermal polarization percentages are increased and show a pronounced maximum at $Az = 150°$. In these sectors $p_{\rm n}(11) < p_{\rm n}(6)$ and $DP_{\rm n}(11,6) < 1$, indicating Faraday depolarization. In the same interval the ordered field strength $B_{\rm ord}$ is increased and $B_{\rm ran}/B_{\rm ord}$ has dropped to $\simeq 1$. In sector $Az = 210°$ $B_{\rm ran}$ suddenly increases by $2\,\mu$G. This is caused by the large H II complex south-west of the nucleus that is visible as a bright source in both thermal and non-thermal intensity (i.e. see Fig. 4). $RM_{\rm i}(11,6)$ is small in all sectors ($< |20|\,{\rm rad\,m^{-2}}$), apart from the sector at $Az = 300°$ where it is strongly negative with nearly $-60\,{\rm rad\,m^{-2}}$. This sector contains a strong decrease in $RM(11,6)$ around RA=$14^h\,02^m\,45^s$, DEC=54° 28′ 35″(see Fig. 11). Here $p_{\rm n}(6)$ and $p_{\rm n}(11)$ reach a minimum of less than 0.1 and $B_{\rm ran}/B_{\rm ord}$ becomes $\simeq 4$. The minimum in the polarization degrees is due to wavelength independent polarization as $p_{\rm n}(6) \simeq p_{\rm n}(11)$.

We discuss the wavelength-independent polarization in the inner ring in the next section. Here we estimate whether Faraday depolarization could explain $p_{\rm n}(6)$ and $p_{\rm n}(11)$ in the sector at $Az = 150°$ in the outer ring, where $DP_{\rm n}(11,6) \simeq 0.8$ (see Fig. 15).

Internal Faraday dispersion usually is the strongest Faraday effect, for which Burn (1966) and Sokoloff et al. (1998) give the expression

$$p_{\rm n}(\lambda) = p_0\,(1 - \exp(-2S))\,/\,2S, \qquad (4)$$

where $S = \sigma^2_{\rm RM}\,\lambda^4$ and $p_0 = 0.75$ is the maximum degree of polarization [5]; $\sigma_{\rm RM}$ is the standard deviation of the intrinsic rotation measure $RM_{\rm i}$. For the wavelengths of $\lambda\lambda$ 6.2 cm and 11.1 cm, we find that $\sigma_{\rm RM} = 40\,{\rm rad\,m^{-2}}$ gives the observed value of $DP_{\rm n}(11,6) \simeq 0.8$. This value of $\sigma_{\rm RM}$ is similar to those in NGC 6946 (Beck 2007) and IC 342 (Beck 2015) of $38\,{\rm rad\,m^{-2}}$ and $55\,{\rm rad\,m^{-2}}$, respectively.

Although $\sigma_{\rm RM} = 40\,{\rm rad\,m^{-2}}$ can explain $DP_{\rm n} = 0.8$, the values of $p_{\rm n}(6) = 0.73$ and $p_{\rm n}(11) = 0.50$ resulting from Eq. 4, are much higher than those observed, which are $p_{\rm n}(6) = 0.39$ and $p_{\rm n}(11) = 0.31$. Therefore, the value of $p_{\rm n} \simeq 0.40$ is the result of wavelength-independent polarization. This rather high value could partly come from anisotropic magnetic fields (Fletcher et al. 2011) (see Sect. 4.2.2). Thus in the sector $Az = 150°$ in the outer ring the combination of Faraday dispersion

[4] Instead of wavelength-independent depolarization we use the more accurate description of wavelength-independent *polarization* (see Sokoloff et al. (1998)), emerging from ordered fields (at small wavelengths) or from sheared or compressed random magnetic fields in the emission region (see Sect. 4.2.2).

[5] $p_0 = (1 + \alpha_{\rm n})/(5/3 + \alpha_{\rm n}) = 0.74 \pm 0.09$ for $\alpha_{\rm n} = 0.92$.

and wavelength-independent polarization can explain the observations, where the latter is the dominant polarization mechanism.

It is interesting to see whether the value of $\sigma_{\rm RM}$ = 40 rad m^{-2} is consistent with the properties of the magneto-ionic medium in M 101. We can estimate $< n_{\rm e} >$, the average electron density along the line of sight (in cm^{-3}), using the relation

$$\sigma_{\rm RM} = 0.81 < n_{\rm e} > B_{\rm ran,a} \sqrt{L_{\rm ion}\, d / f}, \quad (5)$$

where $B_{\rm ran,a}$ is the strength of the component of the isotropic random field along the line of sight (in μG); $L_{\rm ion}$ is the path length through the layer of diffuse gas (in pc) containing ionized cells with a typical size of d = 50 pc, which is the coherence length of turbulence in the ISM (Ohno & Shibata 1993; Berkhuijsen et al. 2006); and f is their volume filling factor along $L_{\rm ion}$. For an exponential scale height of the ionized layer of 1 kpc, $L_{\rm ion}$ = 2000 / cos(i) = 2300 pc, where we assume that we see polarized emission from both sides of the disk. With $B_{\rm ran,a} = B_{\rm ran} \sqrt{1/3}$ = 1.6 μG and f = 0.5 (Berkhuijsen et al. 2006) we find $< n_{\rm e} >$ = 0.06 cm^{-3}, which is about three times higher than found near the sun (Berkhuijsen & Müller 2008). However, a smaller filling factor or a larger size of the ionized cells would bring $< n_{\rm e} >$ closer to the MW value.

Alternatively, we may estimate $< n_{\rm e} >$ from the maximum intrinsic rotation measure in the outer ring using

$$RM_{\rm i} = 0.81 < n_{\rm e} > B_{\rm ord,a} L_{\rm ion}, \quad (6)$$

where $B_{\rm ord,a} = B_{\rm ord} \sin(i)$ is the strength of the ordered magnetic field component along the line of sight, assumed to be regular. With $|RM_{\rm i}|$ = 18 rad m^{-2}, $B_{\rm ord}$ = 3.1 μG (see Fig. 15), and $L_{\rm ion}$ = 2300 pc, we have $< n_{\rm e} >$ = 0.006 cm^{-3}, which is about one-third of the value near the sun. The difference between the two estimates of $< n_{\rm e} >$ suggests that the observed polarized emission mainly travels through thin, diffuse ionized gas, whereas the depolarization by Faraday dispersion is mainly caused by the denser, ionized clouds. However, we should regard this low value of $< n_{\rm e} >$ as a lower limit if part of the ordered field observed in polarized emission is anisotropic (sheared or compressed field), which does not contribute to Faraday rotation and $RM_{\rm i}$ (Fletcher et al. 2011).

We conclude that the low degrees of polarization in M 101 are mainly caused by dispersion of polarization angles by random magnetic fields in the emission regions, leading to wavelength-independent polarization. Faraday dispersion also plays a role, but only in some regions.

4.2.2. What causes wavelength-independent polarization?

In the foregoing Section, we showed that wavelength-independent polarization is the main polarization mechanism in M 101. We now estimate under which circumstances wavelength-independent polarization with $p_{\rm n}$ = 0.1 is obtained in the inner ring (R = 2.′5 - 7.′5) (Fig. 14).

In M 51, Fletcher et al. (2011) found that most of the polarized radio emission from the disk, observed at short wavelengths, arises from anisotropic random magnetic fields that do not contribute to the rotation measure. This may be a general property of galaxy disks, and the low values of $RM_{\rm i}$ in M 101 suggest that anisotropic magnetic fields may be important. Therefore, we discuss two possibilities (recall footnote 2 to Sect. 4.1.1):
(a) polarization by an ordered (regular and/or anisotropic random) field; and
(b) polarization by a purely anisotropic random field.

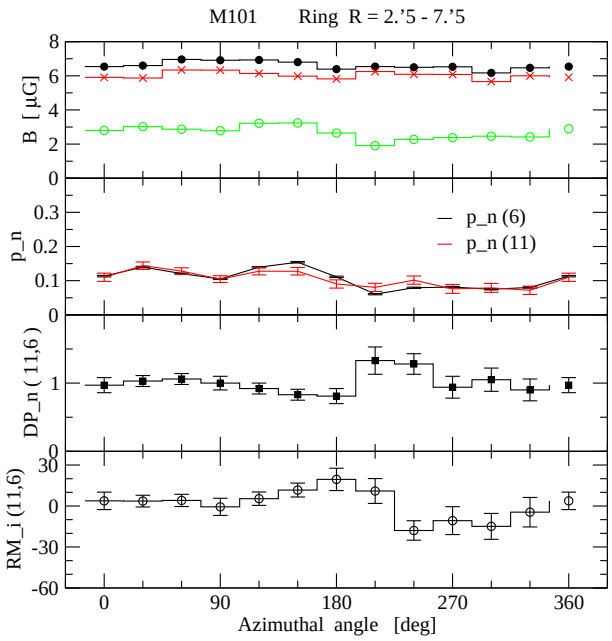

Fig. 14. Variation with azimuthal angle in the plane of M 101 of the mean value of several variables, calculated in 30° -wide sectors in the radial ring R = 2.′5 – 7.′5. The azimuthal angle is counted counter clockwise from the northern major axis. *Top panel*: Equipartition magnetic field strengths $B_{\rm tot}$ (black dots), $B_{\rm ran}$ (red crosses) and $B_{\rm ord}$ (green circles). *Upper middle panel*: Non-thermal polarization percentages $p_{\rm n}(6)$ and $p_{\rm n}(11)$. *Lower middle panel*: Non-thermal depolarization $DP_{\rm n}(11,6)$. *Bottom panel*: Intrinsic rotation measure $RM_{\rm i}(11,6)$. All error bars are statistical errors of one σ. The uncertainty in $\alpha_{\rm n}$ causes systematic errors of 17% in $B_{\rm ord}$, 20% in $p_{\rm n}(6)$, 12% in $p_{\rm n}(11)$, and 10% in $DP_{\rm n}(11,6)$.

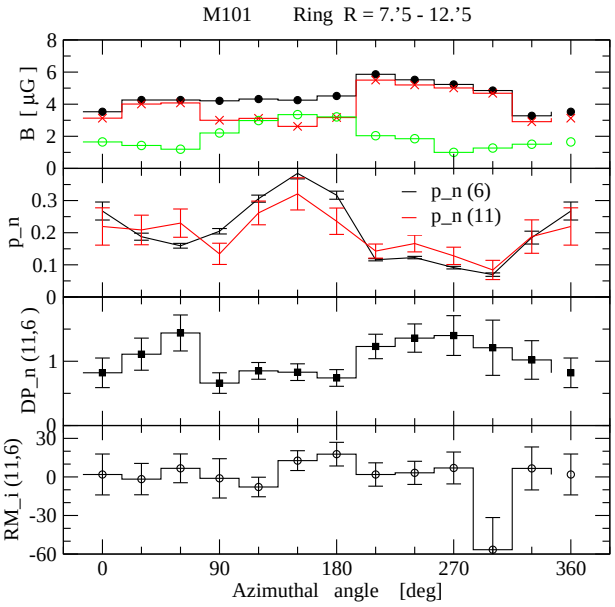

Fig. 15. Same as Fig. 14 for the radial ring R = 7.′5 – 12.′5 in M 101.

For case (a), we use Eq. (24) of Sokoloff et al. (1998) for wavelength-independent polarization in a partly ordered magnetic field,

$$p_{\rm n} = p_0 \frac{B^2_{\rm ord,p}}{B^2_{\rm ord,p} + \sigma^2_{\rm r}}, \quad (7)$$

where p_n is the observed non-thermal degree of polarization, $p_0 = 0.75$ the maximum intrinsic degree of polarization, $B_{ord,p} = B_{ord} \cos(i)$ the strength of the ordered magnetic field component in the sky plane, and σ_r the *standard deviation* of the isotropic random field in the plane of the sky. As σ_r originates from a large number of turbulent cells with a typical size of 50 pc, it does not contribute to the polarized emission. With p_n and B_{ord} known, we can calculate σ_r. [6]

In the inner ring, $B_{ord} \simeq 2.8\,\mu$G (see Fig. 14), and the observed value of $p_n \simeq 0.1$ is reached for $\sigma_r = 5.7\,\mu$G. As the strength of the random field in the plane of the sky is $B_{ran,p} = B_{ran}\sqrt{2/3} = 4.9\,\mu$G, the standard deviation in B_{ran} is about the same as B_{ran} itself, $\sigma_r \simeq 1.2\,B_{ran}$. If part of p_n is due to anisotropic random fields, as addressed in case (b), σ_r is larger than obtained here.

In case (b), we assume that the small degree of polarization in the inner ring entirely emerges from anisotropic random fields (Sokoloff et al. 1998), consisting of many elongated cells causing polarized emission but no rotation measure. This means that the magnetic fields in the emission regions are tangled and disrupted by, for example, stellar winds, supernova shocks, expanding shells, gas outflow from star formation complexes, and Parker loops. By estimating the typical size of the 'cells' of field irregularities, we may identify the main cause of the wavelength-independent polarization.

For a random distribution of polarization angles the number of cells N can be found from (Beck et al. 1999)

$$p_n = p_0\, N^{-0.5}, \tag{8}$$

where p_n is the observed non-thermal degree of polarization, $p_0 = 0.75$ the maximum degree of polarization in an undisturbed regular magnetic field, and N the number of cells in the volume observed. In the inner ring, $p_n \simeq 0.1$ in most sectors (see Fig. 14), giving $N \simeq 60$ in the sector volume. This is a lower limit for N since we know that part of the polarized emission must come from regular magnetic fields causing the observed RM_i.

If a 30° - wide sector contains N cells of size d and a volume filling factor f_v, we obtain

$$N = \frac{f_v\, L_{em}\, ((R_2)^2 - (R_1)^2)\,/\,12}{4/3\,(d/2)^3}, \tag{9}$$

yielding

$$d = [\,f_v\, L_{em}\, ((R_2)^2 - (R_1)^2)/2N]^{1/3}, \tag{10}$$

where L_{em} is the line of sight through the emission region and R_2 and R_1 are the radii determining the inner ring.

The volume filling factor is a combination of the area filling factor f_a and the filling factor along the line of sight $f_L = d\,/\,L_{em}$, $f_v = f_L\, f_a$. Inserting this into the above equation and solving for d again yields

$$d = f_a^{0.5}\,[((R_2)^2 - (R_1)^2)\,/\,2\,N]^{0.5}. \tag{11}$$

Thus d is independent of L_{em} and directly proportional to $N^{-0.5}$. With $R_2 = 16.1$ kpc, $R_1 = 5.4$ kpc, and $N = 60$, we find

$$d \simeq f_a^{0.5}\,1400\,\text{pc}. \tag{12}$$

[6] Equation (7) is valid for a constant value of the density of cosmic ray particles. In case of energy equipartition between cosmic ray particles and magnetic fields, p_n is about 25 % higher than given by Equation 7 (Sokoloff et al. 1998) and σ_r is about 15 % higher than the value we derived here.

As $f_a < 1$, the typical size of the cells of field irregularities responsible for the wavelength-independent polarization may be of the order of 1 kpc, which is much larger than the typical size of 50 pc of supernova remnants. Instead they could be large shells caused by multiple supernova explosions, chimneys of gas rising from star-forming regions, or Parker loops. The frequency and size of chimneys and Parker loops in galactic disks are poorly known (Mao et al. 2015), but large shells and superbubbles have been observed in many galaxies (Bagetakos et al. 2011) and could be an important cause of disordered magnetic fields in galactic disks.

In M 101 Kamphuis (1993) detected 52 H I shells, visible as holes in the H I column density distribution and in position–velocity diagrams. Their diameters range from about 700 pc to about 2500 pc, but many shells below and around the resolution limit of about 500 pc have been missed. In a similar study on NGC 6946 with slightly better resolution, Boomsma et al. (2008) estimated that at least two-thirds of the shells with sizes above the resolution limit had not been detected. If this also holds for M 101, it should at least contain 156 shells with diameters between 500 pc and 2500 pc. This still is a lower limit because well-resolved studies on M 31 (Brinks & Bajaja 1986) and M 33 (Deul & den Hartog 1990) show that the size distribution of H I shells peaks at 200 – 300 pc (see also Bagetakos et al. (2011)).

Kamphuis (1993) calculated the area filling fraction f_a of the observed shells as a function of radius. In the inner ring at R = 5.4 – 16.1 kpc, the mean value of $f_a = 0.16$, which may increase to $f_a = 0.2$ if the missing smaller shells are added. Inserting this into Eq. 12, we find a mean size of the shells causing the wavelength-independent polarization of $d = 625$ pc.

However, $d = 625$ pc is an upper limit because part of the observed polarized emission, and thus of p_n, must come from regular magnetic fields observed as Faraday rotation measures (Fig. 14). If, for example, only half of the polarized emission were due to anisotropic random magnetic fields, reducing p_n to 0.05, the number of cells in a sector would increase to $N = 225$ and their mean diameter would decrease to $d = 320$ pc. This diameter comes close to the most common size of H I shells in well-resolved galaxies.

We conclude that the wavelength-independent polarization in M 101 could partly be due to strong disturbances of the regular magnetic field by explosive events that give rise to H I shells with mean diameters of less than 625 pc.

4.3. Large-scale magnetic field and H I spiral arms in M 101

In this section we investigate the relationship between the large-scale, ordered magnetic field in M 101 and spiral arms seen in Hα and H I by studying the orientation of the magnetic pitch angles, which we calculate from the polarization angles at λ 6.2 cm.

Figure 11 shows that Faraday rotation in M 101 generally does not exceed 30 rad m^{-2}, yielding a maximum rotation angle of 7° at λ 6.2 cm. This rotation angle is comparable to the uncertainty in the polarization position angle, and it only exceeds 40 rad m^{-2} (corresponding to 9°) in small isolated regions. Therefore, we did not correct the polarization angles for the Faraday rotation offset.

Figure 16 shows the large-scale distribution of magnetic pitch angles (defined as the angle between the apparent B-vectors at λ 6.2 cm, corrected for the inclination, and the local azimuthal direction in the disk) and the brightest parts of the H I spiral arms containing star-forming regions. Generally, the pitch angles of the B-vectors are largest in the northern and

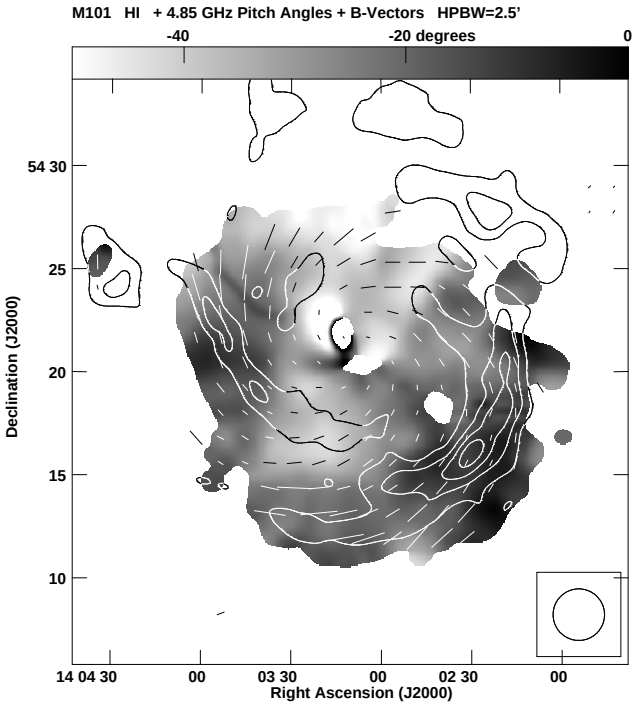

Fig. 16. The magnetic pitch angles in M 101 at λ 6.2 cm shown in greyscale with apparent B-vectors and some contours of the H I spiral arms (Braun 1995) superimposed, smoothed to the beamwidth of 2.′5. The contour levels are (10, 15, 20, and 25) 10^{20} cm^{-2}. The pitch angles are corrected for the inclination of 30° , but not for Faraday rotation because it is < 7° . The pitch angles are smallest in the south-west, where the apparent B-vectors run nearly parallel to the H I arms, but pitch angles near −40° occur in the south and the north. The length of the B-vectors is proportional to the non-thermal degree of polarization with 1′ = 20%.

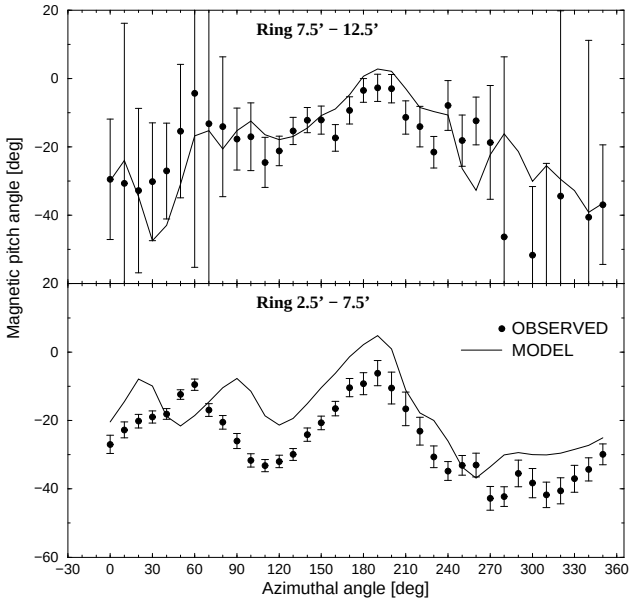

Fig. 18. Variations with azimuthal angle of the magnetic pitch angle in M 101 averaged in 10° sectors in the rings R = 2.′5 − 7.′5 and R = 7.′5 − 12.′5, compared to the variations expected if the magnetic field is aligned with H I of the model filaments. The azimuthal angle is counted counter-clockwise from the NE major axis. The pitch angles are corrected for the inclination as well as for the Faraday rotation.

smallest in the SW region of M 101. They are also very small in the outer part of the southern disk, but become larger towards the centre. While the SW region shows a radial *decrease* of the magnetic pitch angle, the magnetic pitch angle tends to *increase* with radius towards the NW, N, and NE.

There is no clear association of magnetic pitch angles with the star formation distribution in M 101 (compare also Fig. 4). Large pitch angles are found at the position of the extended star-forming complex south of the disk centre as well as in a quiescent outer northern region. There is no clear indication that the ratio of radial-to-azimuthal magnetic field is enhanced close to star-forming regions. One might expect this if the radial field is produced locally out of the azimuthal field by a turbulent dynamo boosted by turbulent activity in actively star-forming portions of the disk.

We checked the hypothesis that the magnetic field orientations in the disk of M 101 may be controlled by compression effects in H I filaments by comparing the orientations of the B-vectors at λ 6.2 cm to those of H I structures (Braun 1995). Figure 17a shows that in the frame of azimuthal angle in the disk – $ln(r)$, where r is the galacto-centric radius, the magnetic field orientations generally follow the H I filaments. The long, weak filament starting at Az = 70° , $ln(r)$ = 2.5 runs parallel to B-vectors. At Az = 150° − 210° , $ln(r)$ > 2, the filament and magnetic field become nearly azimuthal and then they both bend towards smaller $ln(r)$. On the other hand, the B-vectors are apparently inclined with respect to a bright filament crossing the former filament at Az = 210° , $ln(r)$ = 2.1. The magnetic field orientations are well aligned with a prominent H I filament at Az = 30° −90° , beyond which they become inclined to the more diffuse continuation of this filament. At Az > 270° , $ln(r)$ < 2.1, there is good agreement between large magnetic pitch angles and the general preponderance of highly inclined, diffuse H I structures.

Because of significant beam-smearing effects, the question of an agreement or disagreement of observed magnetic pitch angles and the orientations of H I structures must be solved by means of beam-smoothed models of polarized emission. For this purpose, we digitized the loci of maxima of clearly identifiable H I filaments. We ignored localized wiggles that are much smaller than our beam, and traced a general trend of each filament. Each filament was split into segments about 1′ long. The magnetic field was assumed to run locally parallel to each segment. We integrated contributions from particular segments to the Q and U Stokes parameters convolved to a beam of 2.′4 using techniques described by Urbanik et al. (1997) and Soida et al. (1996). To best reproduce the observations, the contributions from particular filament segments were weighted with the polarized intensity observed at this position. Then, we combined the Q and U distributions to a map of polarization angles, and analysed these angles in the same way as the observed angles. As a result of the smoothing procedure polarization angles between H I filaments also occur.

The results are compared to observations in Fig. 17 a, b, and c. The H I filaments and apparent B-vectors show similar large-scale variatons in the pitch angles. The model well reproduces the magnetic field following the long filament running from Az = 70° , $ln(r)$ = 2.5 to Az = 270° close to the centre, and another filament at Az = 30° − 90° . The preponderance of highly inclined B-vectors at azimuths Az > 270° , $ln(r)$ < 2.1 is also well reproduced. However, large differences reaching 30° occur between Az = 90° and Az = 210° at $ln(r)$ < 2. Here M 101 has a significantly inclined magnetic field, but the model predicts an almost azimuthal field. This results from assuming that the magnetic field is parallel to a prominent filament at Az = 130° −240° and to an almost horizontally running fuzzy

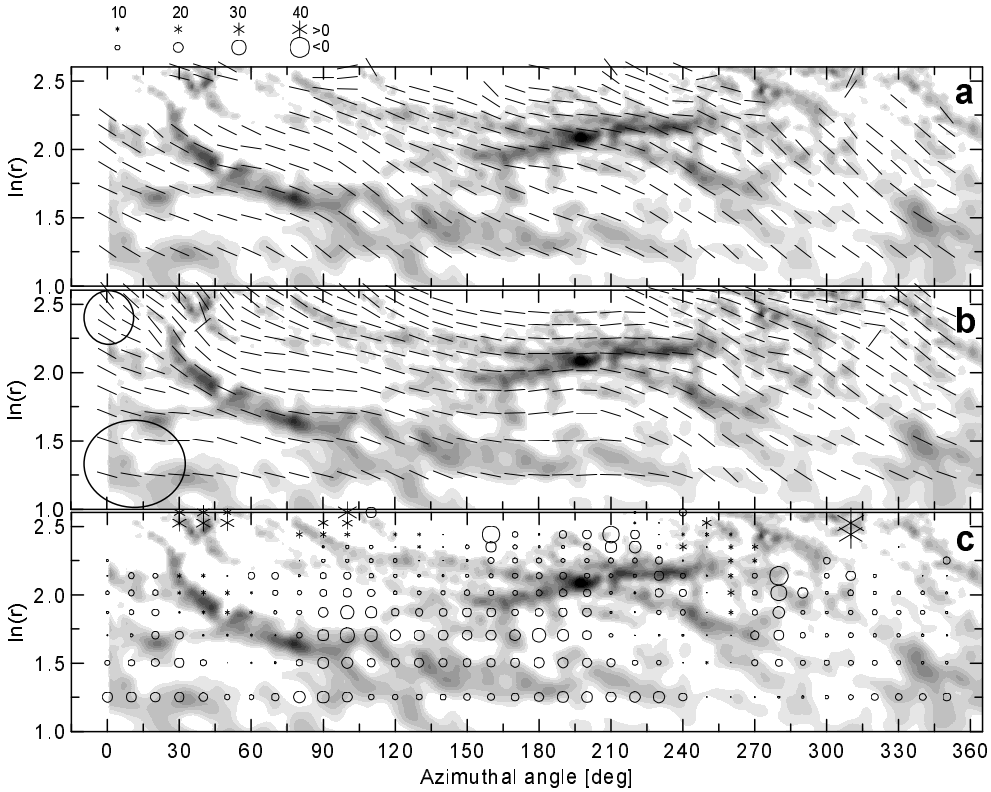

Fig. 17. a) Orientations of the apparent B-vectors (plotted with equal length) in M 101 at λ 6.2 cm (corrected for inclination) in the frame of azimuthal angle in the disk plane and $ln(r)$ (r is the galacto- centric radius in arcmin), overlaid onto the H I distribution of Braun (1995), smoothed to a beamwidth of 20″. **b)** Orientation of the B-vectors (plotted with equal length) of the magnetic field model assuming the magnetic field to be parallel to the H I filaments. Ellipses show the beamwidth at selected radii. **c)** Differences between model and observations shown as symbols with size proportional to the pitch angle difference (the scale is given at the top of the Figure). As the pitch angles are mostly negative, a negative difference means a more inclined B-vector in the observed than in the model map. The azimuthal angle runs counter clockwise from the NE major axis.

structure at $ln(r) = 1.3$. Some large discrepancies at $ln(r) \geq 2.2$ are uncertain because the signal-to-noise ratio in *PI* is low. Thus, in M 101 there are some regions that show a stronger radial magnetic field than one would expect from field lines consistently parallel to the filaments.

The pitch angles are shown in Fig. 18, where corrections for the mean Faraday rotation at given azimuthal angles have been applied. The model and observed magnetic pitch angles vary in a similar way with azimuthal angle, which means that the orientation of H I filaments is efficiently controlling the pitch angle of magnetic fields. There is a clear asymmetry in the pitch angles between the northern ($Az = 0°$) and southern ($Az = 180°$) major axis: The pitch angles in the north are much more negative than in the south. This may be related to the lopsidedness of M 101, the disk of which is much more extended along the northern major axis than along the southern major axis, which is possibly the result of past encounters with members of the M 101 group (e.g. Karachentsev & Kudrya 2014; Mihos et al. 2013; Jog & Combes 2009; Waller et al. 1997). The H I filaments may be associated with density perturbations caused by the encouter(s), aligning the magnetic field like density waves do in spiral arms.

The model magnetic field, based on the H I filaments, generally has smaller pitch angles than are observed (Fig. 18). In the inner ring the unweighted mean difference is $8 \pm 1°$. In the outer ring the difference seems to be smaller but cannot be determined with sufficient accuracy. In the barred spiral galaxy M 83, the magnetic pitch angles are on average about 20° larger than the pitch angles of the material arms traced in CO and H I (Frick et al. 2016).

We suggest that there is a source of radial magnetic fields other than pure compression aligning the field lines with local H I filaments. The large-scale $\alpha - \Omega$ dynamo naturally produces the radial magnetic field component and hence increases the magnetic pitch angle (Beck et al. 1996). The excess of the radial component is strongest in the inter-arm space away from star-forming regions (Fig. 17). The large-scale dynamo process apparently works more efficiently in inter-arm regions, which could be the result of enhanced outflows in the spiral arm regions (Chamandy et al. 2015).

5. Summary

We present observations of total and polarized emission from the spiral galaxy M 101 at $\lambda\lambda$ 6.2 cm and 11.1 cm, which we carried out with the Effelsberg telescope. The angular resolutions are 2.′5 (= 5.4 kpc) and 4.′4 (= 9.5 kpc), respectively. We used these data to study the various emission components and the properties of the magnetic field in M 101 . Our main results are summarized below.

– The thermal radio emission is closely correlated with the spiral arms, but the non-thermal emission is more smoothly distributed indicating diffusion of cosmic ray electrons from their places of origin. The thermal fraction at λ 6.2 cm is $f_{\rm th} < 45 \pm 6\%$ with a systematic error of 10%.

– The radial distributions of thermal and non-thermal emission show a break near $R = 16$ kpc (=7.′4), where they steepen to an exponential scale length of $L \simeq 5$ kpc, which is about 2.5 times smaller than at $R < 16$ kpc. The distribution of the polarized emission has a broad maximum near $R = 12$ kpc and beyond $R = 16$ kpc, this distribution also decreases with $L \simeq 5$ kpc. As near the radius of $R = 16$ kpc the radial distribution of the optical emission also steepens (Mihos et al. 2013) and the position angle, inclination, and the velocity structure of the H I gas change (Kamphuis 1993), a major change in the structure of M 101 must occur near this radius.

– The change in the structure of M 101 near $R = 16$ kpc is also apparent in the radial distributions of the magnetic field strengths $B_{\rm tot}$, $B_{\rm ran}$, and $B_{\rm ord}$. Beyond $R = 16$ kpc their radial scale length is about 20 kpc, which implies that they extend to $R = 70$ kpc before decreasing to 0.3 μG. The strength of $B_{\rm tot}$ ranges from nearly 10 μG at $R < 2$ kpc to 4 μG at $R = 22-24$ kpc. As the random magnetic field dominates in M 101 ($B_{\rm ran}/\,B_{\rm ord} \simeq 2.4$), $B_{\rm ord}$ is weak, varying between 3 μG at $R = 12 - 14$ kpc and 2.1 μG at $R = 22 - 24$ kpc. The mean field strengths for $R < 24$ kpc are $B_{\rm tot} = 6.4\,\mu$G, $B_{\rm ran} = 5.9\,\mu$G, and $B_{\rm ord} = 2.5\,\mu$G.

– The integrated thermal luminosity for $R < 30$ kpc yields a mean SFR per unit area of $\Sigma_{\rm SFR} = 2.5 \pm 0.2\,{\rm M_\odot\,Gyr^{-1}\,pc^{-2}}$, which is somewhat smaller than that of M 33. Averages in 2 kpc-wide rings in the plane of the galaxy decrease from $14\,{\rm M_\odot\,Gyr^{-1}\,pc^{-2}}$ at $R < 2$ kpc to $0.8\,{\rm M_\odot\,Gyr^{-1}\,pc^{-2}}$ at $R = 22 - 24$ kpc. $\Sigma_{\rm SFR}$ and the ring averages have a systematic error of 20%.

– At radii $R < 24$ kpc, the random magnetic field depends on $\Sigma_{\rm SFR}$ with a power-law exponent of $b = 0.28 \pm 0.02$. The systematic error in b is ≤ 0.02.

– In most regions in M 101 rotation measures $RM(11,6)$ are between $-30\,{\rm rad\,m^{-2}}$ and $30\,{\rm rad\,m^{-2}}$, and the non-thermal depolarization $DP_{\rm n}(11,6)$ varies between 0.7 and 1.3.

– Wavelength-independent polarization, caused by the random magnetic field in the emission regions, is the main polarization mechanism in M 101. In some areas beyond $R = 16$ kpc, Faraday dispersion also plays a role. We show that energetic events causing H I shells of several hundred pc in diameter could be responsible for part of the wavelength-independent polarization.

– The ordered magnetic field is generally aligned with the spiral arms showing the same large-scale azimuthal asymmetries, caused by the interaction of M 101 with some of its group members. However, a beam-smoothed model shows that the magnetic pitch angle variations over the disk cannot be entirely caused by alignment of magnetic field lines along H I filaments as there are substantial local deviations. The magnetic pitch angles are on average about 8° larger than the pitch angles of the model H I filaments, indicating the action of a large-scale dynamo.

Acknowledgements. This research has been supported by a scientific grant from the National Science Centre (NCN), dec. No. 2011/03/B/ST9/01859. We thank Dr. Aritra Basu for careful reading of the manuscript and useful comments. We also thank the anonymous referee, whose detailed comments led to several improvements of the text.

References

Bagetakos, I., Brinks, E., Walter, F., et al. 2011, AJ, 141, 23
Beck, R. 2007, A&A, 470, 539
Beck, R. 2015, A&A, 578, A93
Beck, R., Berkhuijsen, E. M., & Uyaniker, B. 1999, in Plasma Turbulence and Energetic Particles in Astrophysics, ed. M. Ostrowski & R. Schlickeiser, 5–17
Beck, R., Brandenburg, A., Moss, D., Shukurov, A. ., & Sokoloff, D. 1996, ARA&A, 34, 155
Beck, R. & Krause, M. 2005, Astronomische Nachrichten, 326, 414
Berkhuijsen, E. M., Beck, R., & Hoernes, P. 2003, A&A, 398, 937
Berkhuijsen, E. M., Beck, R., & Tabatabaei, F. S. 2013, MNRAS, 435, 1598
Berkhuijsen, E. M., Mitra, D., & Mueller, P. 2006, Astronomische Nachrichten, 327, 82
Berkhuijsen, E. M. & Müller, P. 2008, A&A, 490, 179
Bigiel, F., Leroy, A., Walter, F., et al. 2008, AJ, 136, 2846
Boomsma, R., Oosterloo, T. A., Fraternali, F. ., van der Hulst, J. M., & Sancisi, R. 2008, A&A, 490, 555
Braun, R. 1995, A&AS, 114, 409
Brinks, E. & Bajaja, E. 1986, A&A, 169, 14
Burn, B. J. 1966, MNRAS, 133, 67
Chamandy, L., Shukurov, A., & Subramanian, K. 2015, MNRAS, 446, L6
Chyzy, K. T. 2008, A&A, 482, 755
Chyży, K. T., Weżgowiec, M., Beck, R., & Bomans, D. J. 2011, A&A, 529, A94
de Vaucouleurs, G., de Vaucouleurs, A., & Corwin, J. R. 1976, in Second reference catalogue of bright galaxies, 1976, Austin: University of Texas Press.
Deul, E. R. & den Hartog, R. H. 1990, A&A, 229, 362
Emerson, D. T. & Gräve, R. 1988, A&A, 190, 353
Emerson, D. T., Klein, U., & Haslam, C. G. T. 1979, A&A, 76, 92
Fernini, I., Burns, J. O., & Perley, R. A. 1997, AJ, 114, 2292
Fletcher, A., Beck, R., Shukurov, A., Berkhuijsen, E. M., & Horellou, C. 2011, MNRAS, 412, 2396
Frick, P., Stepanov, R., Beck, R., et al. 2016, A&A, 585, A21
Gräve, R., Klein, U., & Wielebinski, R. 1990, A&A, 238, 39
Haslam, C. G. T. 1974, A&AS, 15, 333
Heesen, V., Brinks, E., Leroy, A. K., et al. 2014, AJ, 147, 103
Helfer, T. T., Thornley, M. D., Regan, M. W., et al. 2003, ApJS, 145, 259
Hoopes, C. G., Walterbos, R. A. M., & Bothun, G. D. 2001, ApJ, 559, 878
Horellou, C., Beck, R., Berkhuijsen, E. M., Krause, M., & Klein, U. 1992, A&A, 265, 417
Israel, F. P., Goss, W. M., & Allen, R. J. 1975, A&A, 40, 421
Jarrett, T. H., Masci, F., Tsai, C. W., et al. 2013, AJ, 145, 6
Jog, C. J. & Combes, F. 2009, Phys. Rep., 471, 75
Jurusik, W., Drzazga, R. T., Jableka, M., et al. 2014, A&A, 567, A134
Kamphuis, J. J. 1993, PhD thesis, University of Groningen, (1993)
Karachentsev, I. D. & Kudrya, Y. N. 2014, AJ, 148, 50
Kelson, D. D., Illingworth, G. D., Freedman, W. F., et al. 1996, ApJ, 463, 26
Kenney, J. D. P., Scoville, N. Z., & Wilson, C. D. 1991, ApJ, 366, 432
Klein, U., Wielebinski, R., & Beck, R. 1984, A&A, 135, 213
Kuntz, K. D., Snowden, S. L., Pence, W. D., & Mukai, K. 2003, ApJ, 588, 264
Lee, M. G. & Jang, I. S. 2012, ApJ, 760, L14
Leroy, A. K., Bigiel, F., de Blok, W. J. G., et al. 2012, AJ, 144, 3
Mao, S. A., Zweibel, E., Fletcher, A., Ott, J., & Tabatabaei, F. 2015, ApJ, 800, 92
Mihos, J. C., Harding, P., Spengler, C. E., Rudick, C. S., & Feldmeier, J. J. 2013, ApJ, 762, 82
Mihos, J. C., Keating, K. M., Holley-Bockelmann, K., Pisano, D. J., & Kassim, N. E. 2012, ApJ, 761, 186
Mulcahy, D. D., Horneffer, A., Beck, R., et al. 2014, A&A, 568, A74
Ohno, H. & Shibata, S. 1993, MNRAS, 262, 953
Oppermann, N., Junklewitz, H., Robbers, G., et al. 2012, A&A, 542, A93
Ott, M., Witzel, A., Quirrenbach, A., et al. 1994, A&A, 284, 331
Sandage, A. 1961, in The Hubble atlas of galaxies, 1961, Washington D.C.: Carnegie Institution of Washington.
Scowen, P. A., Dufour, R. J., & Hester, J. J. 1992, AJ, 104, 92
Soida, M., Urbanik, M., & Beck, R. 1996, A&A, 312, 409
Sokoloff, D. D., Bykov, A. A., Shukurov, A., et al. 1998, MNRAS, 299, 189
Suzuki, T., Kaneda, H., Onaka, T., Nakagawa, T., & Shibai, H. 2010, A&A, 521, A48
Tabatabaei, F. S., Beck, R., Krügel, E., et al. 2007a, A&A, 475, 133
Tabatabaei, F. S., Berkhuijsen, E. M., Frick, P., Beck, R., & Schinnerer, E. 2013a, A&A, 557, A129
Tabatabaei, F. S., Krause, M., & Beck, R. 2007b, A&A, 472, 785
Tabatabaei, F. S., Schinnerer, E., Murphy, E. J., et al. 2013b, A&A, 552, A19
Urbanik, M., Elstner, D., & Beck, R. 1997, A&A, 326, 465
van Dokkum, P. G., Abraham, R., & Merritt, A. 2014, ApJ, 782, L24
Van Eck, C. L., Brown, J. C., Shukurov, A., & Fletcher, A. 2015, ApJ, 799, 35
Waller, W. H., Bohlin, R. C., Cornett, R. H., et al. 1997, ApJ, 481, 169
Walter, F., Brinks, E., de Blok, W. J. G., et al. 2008, AJ, 136, 2563
Wardle, J. F. C. & Kronberg, P. P. 1974, ApJ, 194, 249
Zasov, A. V. & Abramova, O. V. 2006, Astronomy Reports, 50, 874